Journal of Nanobiotechnology

RESEARCH

Open Access

Inflammation-targeted nanomedicine prevents tumor metastasis following photodynamic therapy by reversing epithelial-mesenchymal transition and ROS-mediated immunosuppression

Zhengwei Song[1†], Quanwei Sun[1†], Wenshuo Yang[1†], Yunlong Li[1], Chaoyu Hu[1], Chen Chen[1], Kang Liu[1], Wei Shen[1,2,4*], Ye Yang[1,2,4*] and Dengke Yin[1,3,4*]

Abstract

Background Prolonging the duration of photodynamic therapy (PDT) enhances the level of reactive oxygen species (ROS), thereby facilitating tumor ablation. However, our findings indicated that excessive ROS not only induces epithelial-mesenchymal transition (EMT) but also creates an immunosuppressive microenvironment in tumor, thereby triggering tumor metastasis.

Methods We initially developed neutrophil membrane hybrid liposomes (NLs) that can specifically target inflamed tumor tissues following PDT. Then, we utilized NLs to encapsulate the antioxidant nanozyme FeGA and the antiplatelet drug Lysine Acetylsalicylate (LAS), resulting in the formulation NLASF.

Results Experimental results demonstrated that FeGA effectively scavenges ROS, thereby reversing the immunosuppressive microenvironment induced by prolonged PDT. Furthermore, the incorporation of LAS effectively disrupts the interaction between tumor cells and platelets, mitigating tumor EMT and inhibiting hematogenous tumor metastasis. In a breast cancer mouse model, we observed that treatment with NLASF led to a near-complete suppression of tumor lung metastasis following the prolonged PDT. Additionally, the in vivo application of NLASF did not result in any blood toxicity or organ toxicity, highlighting its significant advantages over the free drugs group.

†Zhengwei Song, Quanwei Sun and Wenshuo Yang contributed equally to this work.

*Correspondence:
Wei Shen
wshen@ahtcm.edu.cn
Ye Yang
Y.Yang@ahtcm.edu.cn
Dengke Yin
yindengke@ahtcm.edu.cn

Full list of author information is available at the end of the article

© The Author(s) 2025. **Open Access** This article is licensed under a Creative Commons Attribution-NonCommercial-NoDerivatives 4.0 International License, which permits any non-commercial use, sharing, distribution and reproduction in any medium or format, as long as you give appropriate credit to the original author(s) and the source, provide a link to the Creative Commons licence, and indicate if you modified the licensed material. You do not have permission under this licence to share adapted material derived from this article or parts of it. The images or other third party material in this article are included in the article's Creative Commons licence, unless indicated otherwise in a credit line to the material. If material is not included in the article's Creative Commons licence and your intended use is not permitted by statutory regulation or exceeds the permitted use, you will need to obtain permission directly from the copyright holder. To view a copy of this licence, visit http://creativecommons.org/licenses/by-nc-nd/4.0/.

Conclusions This study provides a novel approach to enhance the efficacy of PDT and successfully suppress PDT-mediated tumor metastasis.

Graphical Abstract

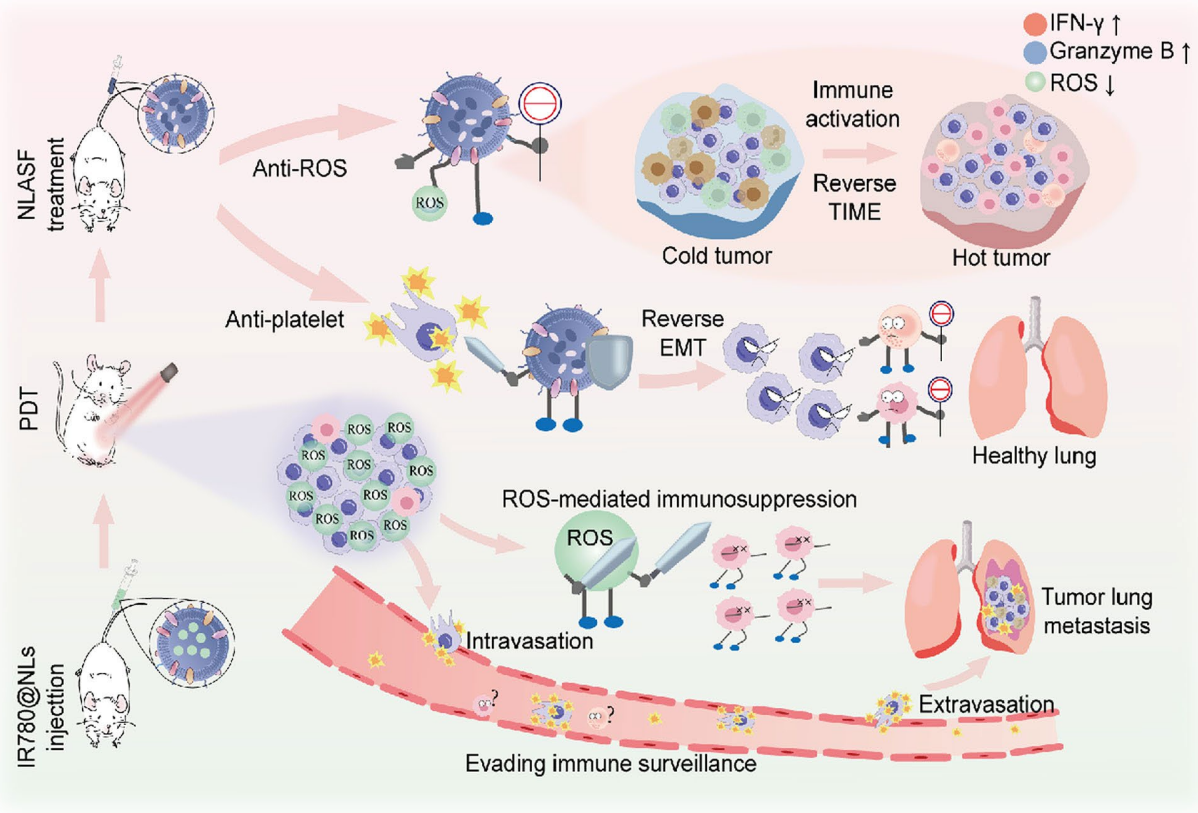

Keywords Reactive oxygen species, Platelet, Neutrophil membrane, Tumor metastasis, Epithelial-mesenchymal transition, Photodynamic therapy

Introduction

Photodynamic therapy (PDT), which utilizes a photosensitizer excited by specific wavelengths, generates a significant amount of reactive oxygen species (ROS) within the target tumor tissue, ultimately leading to cellular death [1]. Obviously, it's common to consider that extending the illumination duration could enhance ROS production, thereby improving the efficiency of tumor eradication. Although ROS makes a significant contribution to tumor ablation, they also pose potential risks [2]. As a double-edged sword, transient exposure to ROS stimulation activates various types of innate and adaptive immune cells. Conversely, sustained exposure to ROS leads to the depletion of antioxidants responsible for maintaining redox balance, ultimately resulting in compromised immune functions and immune suppression [3]. This immunosuppressive microenvironment is characterized by an increase in tumor-supportive myeloid cells (MDSCs), tumor-associated macrophages (TAMs), and regulatory T (T_{reg}) cells, which collectively suppress the activity of cytotoxic T cells and natural killer (NK) cells.

In addition, ROS also act as signaling molecules that drive proliferation and response, facilitating processes such as epithelial-mesenchymal transition (EMT), migration, and adhesion to endothelial cells [4]. Existing studies have shown that the inhibition of catalase within mitochondria significantly enhanced lung metastasis in breast cancer models [5]. Furthermore, employing catalase to eliminate the ROS generated following peritoneal surgery can reduce tumor recurrence [6]. Ishikawa et al. found that preconditioning highly metastatic tumor cells with ROS scavengers significantly attenuated their metastatic capacities within a melanoma model [7]. Thus, we hypothesized that following the use of PDT to generate ROS for the destruction of the primary tumor tissue, the

removal of excess ROS may be advantageous in reversing immune suppression, and preventing tumor metastasis.

Hematogenous metastasis is the most prevalent form of cancer cell dissemination. Therefore, it is essential to consider the intricate relationship between platelets and tumor cells during the process of metastasis through the bloodstream [8]. In 1968, Gasic GJ et al. first proposed the association between platelets and tumor metastasis, suggesting that elevated platelet levels may facilitate tumor metastasis [9]. Specifically, circulating tumor cells (CTCs) promote platelet aggregation, which provides protection to the CTCs. Specifically, most CTCs are destroyed by circulating shear forces and NK cells upon entering the bloodstream, while the surviving CTCs stimulate the activation and aggregation of platelets. By utilizing the physical barrier formed by platelets and their ability to release cytokines that inhibit NK cells, CTCs can evade immune surveillance [10]. Moreover, platelets also can promote tumor progression and metastasis by facilitating the EMT of tumor cells [11]. Therefore, it is reasonable to consider that blocking the interaction between platelet and tumor cells holds promising potential for inhibiting tumor metastasis.

In this study, we first confirmed that extending the duration of PDT for breast cancer results in an increase in the ROS level of tumor region, which subsequently contributes to the establishment of an immunosuppressive microenvironment in the lung and subsequent lung metastasis of breast cancer. Therefore, we aim to combine the antioxidant nanozymes (FeGA, an ultrasmall nanodot with good ROS-scavenging ability) with antiplatelet drugs (Lysine Acetylsalicylate, LAS, a clinical antiplatelet agent) to mitigate the potential of tumor metastasis and recurrence following PDT. Neutrophils can not only target inflamed tumor tissue, but they can also form neutrophil-CTCs clusters with circulating tumor cells. To leverage this property, we developed cell neutrophil membrane hybrid liposomes (NLs) derived from neutrophil membranes, which possess surface membrane proteins similar to those of the source cells. We further co-extruded NLs with LAS and FeGA to produce drug-loaded NLs (referred to as NLASF), thereby achieving efficient targeted delivery of FeGA and LAS to the inflamed tumor tissues following prolonged PDT. Our results revealed that NLASF successfully reversed the immunosuppressive tumor microenvironment through scavenging excessive ROS, thereby converting cold tumors into hot tumors and inhibiting tumor recurrence following prolonged PDT. Furthermore, NLASF considerably hindered platelet aggregation and inhibited the occurrence of EMT in tumor, thereby significantly preventing the tumor metastasis. In short, we provided a combination therapy nanoplatform capable of achieving multiple objectives, ultimately inhibiting tumor recurrence and metastasis after prolonged PDT (Fig. 1). This research offers a promising solution for enhancing the efficacy of PDT and mitigating its adverse prognoses.

Methods

Materials and reagents

1,2-Distearoyl-sn-glycero-9213-phosphoethanolamine-Poly (ethylene glycol)-2000 (DSPE-PEG-2000) (S25991-500 mg), Cholesterin (B61373), LAS (S26232-1 g), 1,1'-Dioctadecyl-3,3,3',3'-Tetramethylindotricarbocyanine Iodide (DiR) (Y18318-5 mg), IR780 iodide (T21162) and Gallic acid (S30153-100 g) were obtained from Yuanye Biotechnology Co., Ltd (China). Egg Yolk Lecithin (P3556) was purchased from Sigma-Aldrich (USA). Commassie Blue Fast Stain Solution (EC0021-A), 3,3'-dioctadecyloxacarbocyanine perchlorate (DiO) (SJ-MD0236), 1,1'-dioctadecyl-3,3,3',3'-tetramethylindocarbocyanine perchlorate (Dil) (SJ-MD0232), Color-enhanced protein molecular marker (EC0019), 4',6-Diamidino-2-phenylindole (DAPI) (EE0011-B), Bovine serum albumin (BSA) (ED0017-A), Rabbit Anti-Goat IgG (H + L)-Alexa Fluor 488 (EF0009), Luminol (SJ-MD0050), Cell Counting Kit-8 (CCK-8) (CT0001-B), Roswell Park Memorial Institute (RPMI) 1640 Medium (CF0002), Dimethyl sulfoxide (DMSO) (CS0001) and 10% sodium dodecyl sulfate polyacrylamide gel electrophoresis (SDS-PAGE) preparation kit (EC0023) were purchased from Sparkjade Biotechnology Co., Ltd (China). Fetal Bovine Serum (FBS) (BC-SE-FBS07) and Dulbecco's modified Eagle's medium (DMEM) high glucose (BC-M-005-500mL) were purchased from Nanjing BioChannel Biotechnology Co., Ltd (China). D-Luciferin sodium salt (D115509-1 g) was purchased from Aladdin reagent Co., Ltd. (China). Singlet Oxygen Sensor Green Fluorescent (SOSG) probe, Penicillin-Streptomycin Solution (C0222), 4% Paraformaldehyde Fix Solution (P0099), 0.25% trypsin-ethylenediaminetetraacetic acid (EDTA) (C0201-100mL) and Membrane and Cytosol Protein Extraction Kit (P0033) were purchased from Beyotime Biotechnology Co., Ltd (China). FITC-conjugated anti-mouse CD3 (100203), PE-conjugated anti-mouse CD3 (300407), PE-conjugated anti-mouse CD4 (100407), PerCPCy5.5-conjugated anti-mouse CD4 (100432), PerCPCy5.5-conjugated anti-mouse CD8 (100731), FITC-conjugated anti-mouse CD8 (344704), PerCPCy5.5-conjugated anti-mouse Granzyme B (GZMB) (372211), APC-conjugated anti-mouse Interferon-gamma (IFN-γ) (505810), PE-conjugated anti-mouse CD11b (101207), FITC-conjugated anti-mouse CD11b (101205), APC-conjugated anti-mouse F4/80 (123115), APC-conjugated anti-mouse Ly-6G/Ly-6 C (Gr-1) (108411), Pacific Blue-conjugated anti-mouse Ly-6G/Ly-6 C (Gr-1) (108429), Alexa Fluor®647-conjugated anti-mouse Forkhead box protein P3 (FOXP3) (108408), APC-conjugated anti-mouse FOXP3 (505809), were purchased

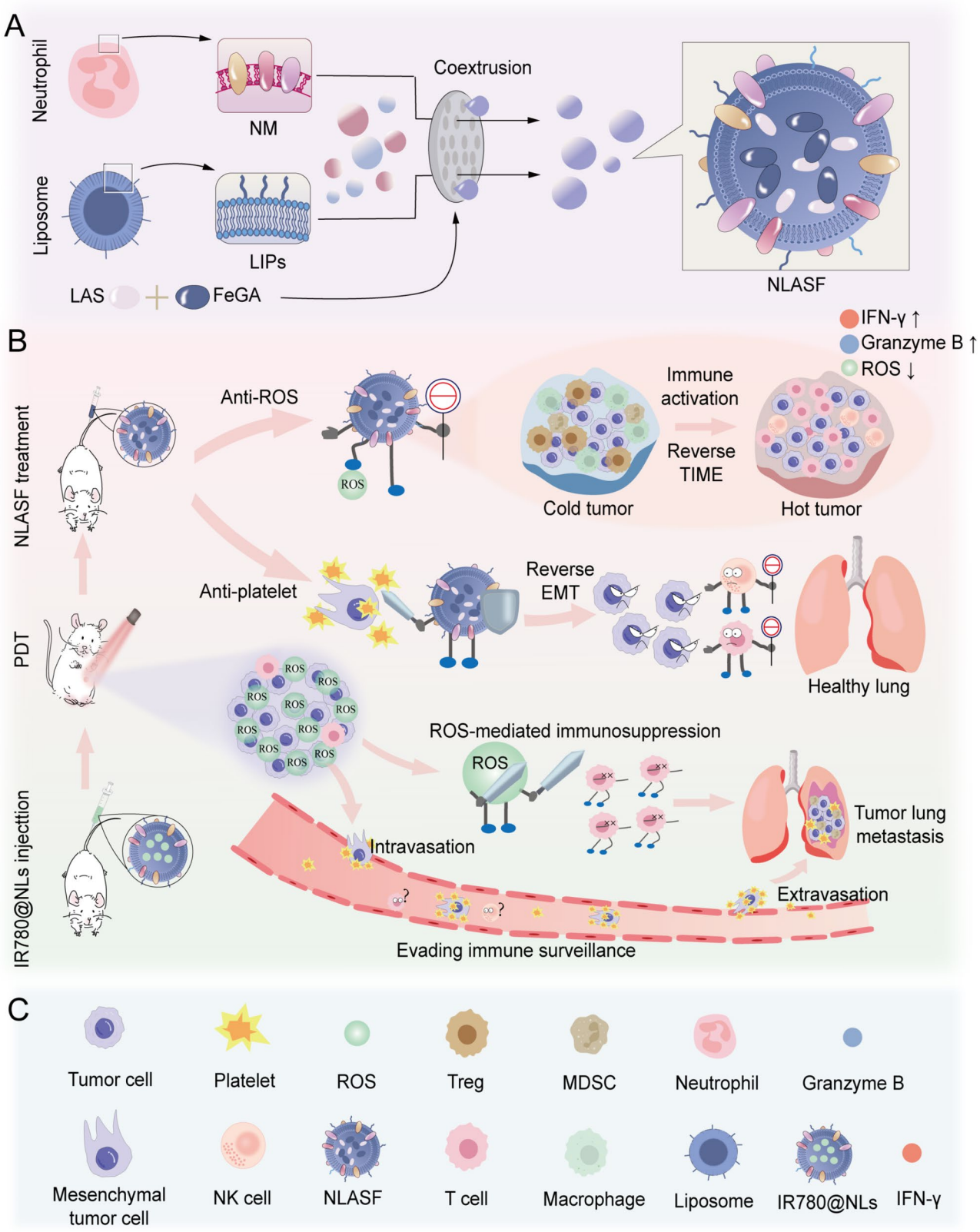

Fig. 1 Schematic illustration of the synthesis of NLASF and using NLASF to inhibit tumor recurrence as well as metastasis following prolonged PDT. (**A**) Synthesis of FeGA and LAS co-loaded cell membrane hybrid liposomes (NLASF). (**B**) Diagrammatic sketch of the therapeutic mechanism of NLASF following prolonged PDT. (**C**) Elements annotation of schematic illustration

from BioLegend (USA). PE-conjugated anti-mouse NK1.1 (70-F2116102-100) and FOXP3/Transcription Factor Staining Buffer kit (IC001-100) were purchased from Multisciences Biotech Co.,Ltd (China). Superoxide Dismutase (SOD) WST-8 Assay kit (JL-T0781), Malondialdehyde (MDA) Assay kit (JL-T0761) and Iron content detection kit (ferrozine colorimetric method) (JL-T1115) were purchased from Jianglai Biotechnology Co., Ltd (China) E-cadherin Polyclonal Antibody (YT1454) and Vimentin Polyclonal Antibody (YT4880) were purchased from ImmunoWay Biotechnology Company (USA). Adenosine Diphosphate (ADP) solution (TOP0849) was purchased from Beijing biotopped Technology Co., Ltd. 2,2-Diphenyl-1-picrylhydrazyl (DPPH), 98% (960333) and 2,2'-Azino-bis(3-ethylbenzothiazoline-6-sulfonic acid) diammonium salt (ABTS), 98% (185223) were purchased from J&K Scientific Co., Ltd. 3,3',5,5'-Tetramethylbenzidine (TMB) (T818493-1 g), Iron(III) chloride hexahydrate ($FeCl_3{\cdot}6H_2O$, I809489-100 g), Polyvinylpyrrolidone (PVP) (molecular weight = 8,000 $g{\cdot}mol^{-1}$, P816206–100 g) andBicinchoninic acid (BCA) Protein Assay Kit (P930762-50T/EA) were purchased from Shanghai Macklin Biochemical Technology Co., Ltd.

Cell lines

All cell lines, including 4T1-Luc (4T1-Luciferase, mouse breast cancer cell line expressing firefly luciferase), Human Promyeloid Leukemia (HL-60) cells and human umbilical vein endothelial cells (HUVEC) were obtained from the Shanghai Cell Bank of the Chinese Academy of Sciences. 4T1-Luc and HL-60 were cultured in RPMI-1640 cell culture medium containing 10% FBS and 1% penicillin-streptomycin. HUVEC were were maintained in DMEM medium with the same formula. The single cell suspension harvested from spleens of mice were maintained in RPMI-1640 cell culture medium containing 10% fetal bovine serum and 1% penicillin-streptomycin. All cell lines was cultured in a humidified 37 °C incubator with 5% CO_2.

Preparation of NLASF

Synthesis of nanozyme FeGA: the $FeCl_3$ solution (100 $mg{\cdot}mL^{-1}$) was added to PVP 8000 solution (100 mg PVP in 10 mL water) for 1 h. Then GA solution (10 $mg{\cdot}mL^{-1}$) was added and stirred overnight. The solution was dialyzed in deionized water for 24 h to remove excess Fe^{3+} and stored at 4℃.

Extraction of the neutrophil membrane (NM): HL-60 cells were cultured in RPMI1640 with 10% (v/v) FBS and 1% (v/v) penicillin-streptomycin. To differentiate HL-60 cells, 1.25% (v/v) DMSO were added in the medium and cells were cultured for 10 days. Differentiated HL-60 cells were re-suspended in phosphate buffered solution (PBS), and then added membrane protein extraction reagent A containing Phenyl methane sulfonyl fluoride (PMSF) to the differentiated HL-60 cells. Following ice bath 15 min, The cell suspension was repeatedly freeze-thawed with liquid nitrogen. The resulting suspension was centrifuged at 14,000 g for 30 min to remove nuclei. Utilizing PBS to resuspend the NM.

Synthesis of liposomes (LIPs): Dissolving DSPE-PEG-2000, egg yolk lecithin, and cholesterol in anhydrous ethanol, gradually add the solution to PBS at a temperature of 55 ℃. After 3 h mixture, the LIPs were obtained.

The extracted NM and LIPs were coextruded with LAS and FeGA. After ultracentrifugation, the NLASF were obtained.

Tumor-targeting and biodistribution of NLs in vivo

To investigate the tumor-targeting effect and biodistribution of NLs, we established orthotopic 4T1-Luc tumor model, female BALB/C mice were subcutaneously injected 4T1-Luc cells (2×10^5 per mouse) into the left mammary gland of mice. Then, all mice were divided into four groups, including (1) LIPs@DiR; (2) PTT + LIPs@DiR; (3) NLs@DiR; (4) PTT + NLs@DiR. When the tumor volume was closed to 200 mm^3, the mice were intravenously injected with various prearations (100 μL per mouse). At predetermined time points (0 h, 1 h, 2 h, 4 h, 8 h, 12 h, 24 h, 48 h, 96 h), all groups of mice were anaesthetized and imaged by in vivo imaging system (IVIS) spectrum system. At 96 h post-injection, all groups of mice were sacrificed. Then, the tumor tissues were taken out for fluorescence imaging and quantitatived by the IVIS spectrum system.

SOSG assay

Tumor tissues were harvested and stored in a -80 ℃ freezer overnight. Then, they were processed in frozen sections. The sections were fixed with 4% paraformaldehyde. After washed with PBS, the sections were reacted with the SOSG probe for 1 h. Following mounting, the sections were the fluorescence images were captured via a confocal laser scanning microscopy (CLSM) system.

Immunofluorescence

In vitro studies, 4T1-Luc cells were seeded in a 24-well plate with cell smears. After various treatments, cells were firstly washed with PBS, and fixed with 4% paraformaldehyde. Then, they were blocked with 5% BSA for 1 h at room temperature, then cells were probed with primary antibody E-cadherin and Vimentin (1:200 dilution) at 4℃ overnight, then incubated with the fluorescently conjugated secondary antibody AF488 (1:1000 dilution) for 2 h at room temperature in the dark and finally stained with DAPI. After mounting, the Immunofluorescence images were captured via a CLSM system. In vivo

studies, tumor tissues were harvested and processed in paraffin sections. Then, Repeat the above steps, and the fluorescence quantification was performed by the image J software.

Platelet isolation and labeling

Whole blood was collected from the orbit of BALB/C mice into a centrifuge tube containing acid-citrate-dextrose (ACD) anticoagulant (85 mM sodium citrate, 65 mM citric acid, 110 mM dextrose) at a 1:9 v/v ratio to the whole blood. Then, the whole blood was centrifuged for 15 min at 1000 rpm at room temperature, and the supernatant was acquired to obtain platelet-rich plasma (PRP). Next, the PRP was centrifuged for 10 min at 3500 rpm, and the platelet sediment was acquired. The supernatant platelet-poor plasma (PPP) was removed. The platelet sediment was gently washed twice with PBS (pH 7.4) and then resuspended in PBS for further use. Fluorescence-labeled platelet was obtained by incubating platelet with DiI (5 $\mu g \cdot mL^{-1}$ in DMSO) for 30 min at 37 ℃.

Transwell assay

The migration and trans-endothelial migration ability of 4T1-Luc cells were evaluated by the transwell assay. For migration assay, after being digested and washed with a serum-free medium, the 4T1-Luc cells were plated into the upper chamber of 8-μm pore filters (300 μL, $8 \times 10^4 \cdot well^{-1}$), which were placed in a 24-well plate with 700 μL of RPMI 1640 medium containing 10% FBS and 1% penicillin-streptomycin solution. 4T1-Luc cells then were treated with PBS, platelet, platelet and various treatments (platelet: 8×10^6, preparations containing LAS: 50 $\mu g \cdot mL^{-1}$, preparations containing FeGA: 50 $\mu g \cdot mL^{-1}$) for 24 h. Then, the insets were washed with PBS (pH 7.4) and the migrated cells were fixed with 4% paraformaldehyde, and the migrated cells were stained with crystal violet (1 $mg \cdot mL^{-1}$) for 15 min, then observed under a inverted microscope. For trans-endothelial migration assay, HUVEC cells (100 μL, $1 \times 10^4 \cdot well^{-1}$ maintained in DMEM medium) were seeded into the upper chamber of 8-μm pore filters and cultured at 37 ℃ to form endothelial cell layers. Then, the 4T1-Luc cells were plated into the upper chamber of 8-μm pore filters (200 μL, $9 \times 10^4 \cdot well^{-1}$), while the lower chamber was supplemented with 700 μL RPMI 1640 medium containing 10% FBS and 1% penicillin-streptomycin solution. After various treatments, (refer to the migration assay) and co-incubation for 24 h, following the same staining procedure as the migration assay, the migrated 4T1-Luc cells were then observes with an inverted microscope.

To investigate the effect of ROS on tumor migration, We similarly applied the transwell assay. the 4T1-Luc cells were plated into the upper chamber of 8-μm pore filters (4T1-Luc $8 \times 10^4 \cdot well^{-1}$), which were placed in a 24-well plate with 700 μL of RPMI 1640 medium containing 20% FBS and 1% penicillin-streptomycin solution. Then, 4T1-Luc cells were treated with PBS, T cells ($5 \times 10^5 \cdot well^{-1}$), H_2O_2 (200 μM), and other various treatments for 24 h (Preparations containing LAS: 50 $\mu g \cdot mL^{-1}$, preparations containing FeGA: 50 $\mu g \cdot mL^{-1}$). Following the same staining procedure as the migration assay, the migrated 4T1-Luc cells were then observes with an inverted microscope.

Platelet aggregation assay

Platelet suspensions were treated with PBS (pH 7.4), or other drug-containing solution for 30 min at 37 ℃ (Platelet: 5×10^7, LAS: 50 $\mu g \cdot mL^{-1}$, FeGA: 50 $\mu g \cdot mL^{-1}$). The solutions were then added with ADP (50 μM) or not and co-incubated for 20 min at 37 °C to induce platelet aggregation, and platelet was labeled with DiI for further observation of their aggregation. Subsequently, the fluorescence images were captured via fluorescence microscopy. The fluorescence quantification was performed by the image J software.

In vitro platelet-tumor cell adhesion assay

To observe the adhesion of platelets to tumor cells, 4T1-Luc cells were seeded onto cell slide 14 mm and grown until confluent. The 4T1-Luc cells then were incubated with PBS (pH 7.4), platelet, and various preparations. After 24 h, cells then were washed with PBS, fixed with 4% paraformaldehyde and nuclei were stained with DAPI. The platelet adhered to tumor cell images were acquired under a CLSM system. The fluorescence quantification was performed by the image J software.

Antioxidant capacity in vitro

For DPPH assay, reaction was performed with various concentrations of NLASF or nanozyme FeGA (0, 25, 50, 100, 160, 250 μg/mL) mixed with DPPH ethanol solution (200 μM), and the absorption of DPPH at 517 nm was detected after 30 min. Scavenging efficiency (%) = $(A_{DPPH}\text{-}A_{sample})/A_{DPPH}) \times 100\%$. A_{DPPH} is the absorption of a pure DPPH ethanol solution. A_{sample} is the absorption of the solution after adding NLASF.

For ABTS assay, reaction was performed with various concentrations of NLASF or nanozyme FeGA (0, 5, 10, 25, 50, 100 μg/mL) mixed with ABTS solution (200 μM, ABTS (4 mM) was activated with potassium persulfate (2.45 mM) overnight, diluted 20 times), and the absorption of ABTS at 734 nm was detected after 30 min. Scavenging efficiency (%) = $(A_{ABTS}\text{-}A_{sample})/A_{ABTS}) \times 100\%$. A_{ABTS} is the absorption of a pure ABTS solution. A_{sample} is the absorption of the solution after adding NLASF.

For TMB probe was applied to test the scavenging effect of NLASF on hydroxy radical (·OH). We configured the TMB probe (19.2 mg/mL, 100 μL) and acquired

the oxTMB reagent by blending it with H_2O_2 (10 mM, 100μL) and $FeCl_2$ (2 mg·ml^{-1}, 100μL), reactions of various concentrations NLASF or nanozyme FeGA were performed for 30 min. After that, The absorption of oxTMB was tested at 640 nm. ·OH scavenging efficiency (%) = $((A_{oxTMB-}A_{sample})/A_{oxTMB}) \times 100\%$. A_{oxTMB} is the absorption of pure oxTMB solution. A_{sample} is the absorption of the solution after drug administration.

Cell viability assay

CCK-8 method was used to measure the viability of T cells, 4T1-Luc cells and HUVEC following various treatments. Cells were inoculated in a 96-cell plate (1×10^4 cells mL^{-1}), and all wells were administered respectively. Quantitative data were acquired by measuring 450 nm absorbance via a microplate reader.

Tumor models

Five weeks old female BALB/c mice were provided by the Animal Center of Anhui University of Chinese medicine. The 4T1-Luc mice tumor model was established by subcutaneous injected 4T1-Luc cells (2×10^5 per mouse) into the mammary gland of mice. When the volume of the tumor increased to ≈130 mm^3, PDT was performed on the tumor-bearing BALB/C mice. Animal experiments are divided into two steps. Step 1: tumor-bearing mice were randomly divided into four groups, including (1) Control, (2) 10 min, (3) 15 min, (4) 20 min. Utilizing various duration PDT for each mice. All groups of mice were intravenously injected with IR780@NLs (100 μL), and all mice were either irradiated with the 808 nm laser (2.0 W cm^{-2}) or not. After PDT or not, the 4T1-Luc cells (2×10^5 per mouse) were injected in the tail vein of each tumor-bearing BALB/C mice. On day 8, the residual tumor tissues were harvested; on day 16, lung tissues were harvested. Step 2: tumor-bearing mice were randomly divided into six groups, including (1) PBS (G1), (2) LAS/FeGA (G2), (3) LAS@NLs (G3), (4) FeGA@NLs (G4), (5) LAS@FeGA@LIPs (G5), (6) NLASF (G6). All groups of mice were intravenously injected with IR780@NLs (100 μL), and all mice were either irradiated with the 808 nm laser (2.0 W cm^{-2}) or not. After prolonged PDT, the 4T1-Luc cells (2×10^5 per mouse) were injected in the tail vein of each tumor-bearing BALB/C mice. Then, the various formulations (100 μL per mouse) were injected into the tail vein. Formulations contained FeGA were 5 mg ml^{-1} in G2, 4, 5, 6. while the concentration of LAS were 2.0 mg ml^{-1} in G2, 3, 5 and 6. The various formulations were administered every two days, starting from day 0, for three doses. The tumor tissues and lung tissues were acqired on day 8 and day 16. The tumor sizes and body weight were recorded every 2 days from day 2 to day 16.

In vivo biosafety evaluation

The tail bleeding time evaluation assay was first conducted to explore whether the NLASF could cause a risk of bleeding. One hour after the last treatment to 4T1-Luc orthotopic tumor-bearing mice, the tail of each mice were submerged in PBS (pH 7.4) at 37 °C, immediately following cuting 3 mm from the tip of the tail using a scalpel. The tail bleeding time was defined as the duration from the removal of the tail to bleeding cessation. Moreover, at the end of treatments, whole blood was harvested for hematology analysis. Determined the levels of aspartate aminotransferase (AST) and alanine aminotransferase (ALT) in plasma, using AST and ALT assay kit respectively.

Statistical analysis

All data presented in this paper are reported in the format of means ± standard deviation (SD), and are based on at least three experiments. The differences between two independent groups were examined using a T-test, while the statistical analysis among multiple groups was conducted using one-way analysis of variance (ANOVA), using origin 2019 software. A value of $P < 0.05$ was considered to be significant difference.

Results and discussions

Prolonged PDT generated high level of ROS and exacerbated lung metastasis

In order to evaluate the impact of PDT duration, we established a tumor model by orthotopically inoculating 4T1-Luc into BALB/C mice. Once the orthotopically implanted tumor size reached around 130 mm^3, each group was subjected to PDT for different durations (Divided into four groups: Control, 10 min, 15 min, 20 min). To enhance the targeted delivery of the photosensitizer IR780, we prepared IR780-loaded NLs (IR780@NLs) for use in PDT. After PDT of different durations, tumor tissues and lung tissues were harvested on day 8 and 16 (Fig. 2A). It was observed that extending the PDT duration resulted in a more complete ablation of primary tumors (Figure S1). Our experimental results further indicated that prolonged PDT has induced elevated levels of MDA [12] (Fig. 2B) and decreased levels of SOD, suggesting an increased oxidative stress [13] (Fig. 2C). Myeloperoxidase (MPO) is a peroxidase primarily produced in neutrophils. MPO-derived oxidants have been proved to be relevant to tissue damage and immune system [14]. Bioluminescence imaging revealed that the bioluminescence signal of MPO probe (luminol [15]) in the long-term irradiation group exhibited increased intensity (Fig. 2D and S2). Furthermore, CLSM images showed that the fluorescent intensity of singlet oxygen($^1O_2$) probe (SOSG [16]) within the tumor tissue section increased with the prolonged duration of PDT.

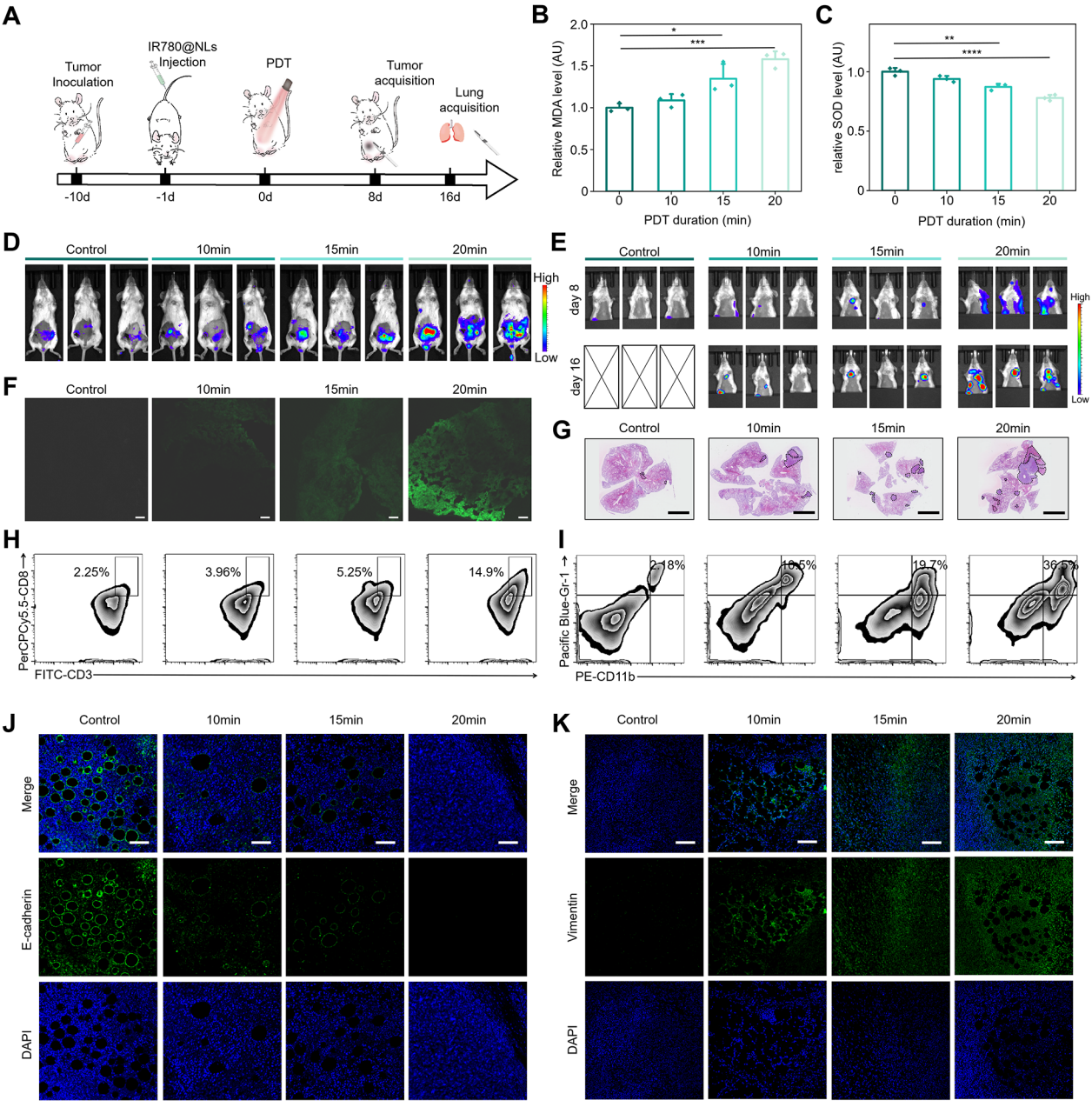

Fig. 2 Biological effects of the various duration of PDT. (**A**) Animal experiment Diagrammatic sketch of tumor-bearing mice with various duration PDT. (**B**) Relative MDA level of tumor tissue homogenate following various PDT ($n = 3$). (**C**) Relative SOD level of tumor tissue homogenate following various PDT ($n = 3$). (**D**) Luminol bioluminescence imaging of MPO level following various duration PDT. (**E**) Bioluminescence images of pulmonary metastasis on days 8 and 16 from mice in each group. (**F**) Fluorescence tissue image via SOSG probe indicated ROS generated by various duration PDT. Scale bar = 50 μm. (**G**) Representative H&E staining analysis of lung tissues treated with various duration PDT. Scale bar = 5 mm. (**H**) Flow analysis of $CD3^+CD8^+$ cells infiltration in tumor tissues after various duration PDT. (**I**) Flow analysis of $CD11b^+Gr\text{-}1^+$ cells infiltration in lung tissues after various duration PDT. Representative fluorescence images of tumor-bearing BABL/C mice following various duration PDT. Staining of (**J**) E-cadherin and (**K**) Vimentin (both green). DAPI (blue) for staining nucleus. Scale bar = 100 μm. [Legend: (*) $p < 0.05$, (**) $p < 0.01$, (***) $p < 0.001$, and (****) $p < 0.0001$]

(Fig. 2F). H&E analysis of tumor tissue illustrated that the extended duration of PDT resulted in exacerbated formation of tumor thrombus, suggesting the aggregation of platelets (Figure S3). Sixteen days post-PDT, bioluminescence images revealed that metastasis occurred to a certain extent in the control group, with the severity of lung metastasis progressively worsening as the duration of PDT increased (Fig. 2E). H&E-stained lung sections further corroborated this result (Fig. 2G).

Moreover, we have conducted initial immunodetection on tumor and lung tissues. $CD8^+$ T cells are particularly important because they can directly kill tumor cells. Our results indicated that $CD3^+CD8^+$ T cells [17] in tumor tissues were upregulated with the extension of PDT (Fig. 2H). In addition, we detected the expression of MDSCs in the lungs, which play a significant role in establishing pulmonary metastatic niches, promoting immunosuppression, and assisting tumor cells in evading immune surveillance. Flow cytometry analysis indicated higher proportion of MDSCs [18] in lung tissue of the long-term irradiation group, suggesting the establishment of an immunosuppressive pulmonary metastatic niches (Fig. 2I). According to the above results, we found that although prolonged PDT can increase T cell infiltration in the primary tumor site, lung metastasis was exacerbated, suggesting that the function of anti-tumor immune cells within lung tissues was probably inhibited by excess ROS. Moreover, immunofluorescence images illustrated that extending the PDT duration lead to the upregulation of Vimentin and downregulation of E-cadherin [19] (the primary hallmarks of EMT). These results suggested the tumor tissues in the long-term irradiation group are undergoing a transition towards a more invasive mesenchymal phenotype (Fig. 2J K).

Preparation and characterization of NLASF

To Fabricate NLASF, we selected HL-60 cells and induced it's differentiation into neutrophils. Flow cytometry analysis revealed that over 95% of the HL-60 cells expressed positive CD11b and Gr-1 after the stimulation of 1.25% DMSO, which are markers of neutrophils (Figure S4). This indicates that HL-60 cells were successfully differentiated into neutrophils. Utilizing membrane extraction kit, we acquired NM [20]. Subsequently, we employed PVP 8000 as a stabilizer, while gallic acid and Fe^{3+} were chosen as organic ligand and inorganic crosslinking agents, respectively. This approach successfully facilitated the synthesis of nanozyme FeGA, which is designed to scavenge ROS [21]. High-resolution transmission electron microscopy (HRTEM) revealed that FeGA were spherical with superior dispersibility, ranging from 5 to 9 nm (Figure S5). Then, ethanol injection method was employed for the preparation of LIPs. Furthermore, the mixture of FeGA, LAS [22], LIPs, and NM underwent repeated extrusion through 200 nm polycarbonate membranes to control particle size, resulting in stable and uniform biomimetic fusion membrane-coated nanodrugs, referred to as NLASF. The dynamic light scattering (DLS) results showed that the size of NLASF in water was about 181.5 nm, which was 57 nm larger than LIPs (Fig. 3A). And the zeta potential of NLASF was -22.0 ± 0.3 mV, which was significantly lower than that of LIPs (Fig. 3B). SDS-PAGE analysis demonstrated that NLs and NM exhibited similar protein expression, indicating that the NLs retained relatively intact neutrophil proteins. Quantitative analysis further revealed that no significant loss of neutrophil membrane components (Fig. 3C). The encapsulation efficiency of LAS and FeGA were both exceeded 80%, as determined by high-performance liquid chromatography (HPLC) and iron content analysis, respectively (Figure S6). To demonstrate the confusion between LIPs and NM, as well as the tumor-targeting capability of NLs in vitro, the NM and LIPs were labeled with DiO (green) and DiI (red), respectively [23]. After coextrusion, NLs which were labeled by DiO and Dil were obtained. After labeled NLs, LIPs, and NM were respectively co-incubated with 4T1-Luc cells for 4 h, the CLSM images revealed that, after coextrusion, there was significant overlap between the green (DiO) and red (DiI) fluorescence in NLs, suggesting the successful confusion of the LIPs and NM. In addition, the red fluorescence signal in the NLs group is prominently observed in the tumor cells, whereas the red fluorescence in the tumor cells of the LIPs group is significantly weaker. This phenomenon suggested that the prepared NLs preserve the tumor-targeting capability of NM (Fig. 3D). Transmission electron microscopy (TEM) revealed that the shape of NLASF was spherical and similar to that of LIPs. Energy-dispersive X-ray spectroscopy (EDS) mapping images showed that the uniform distribution of elements Fe, N, and O throughout NLASF (Fig. 3E). These results revealed that we have successfully developed a nanomedicine with high drug-loading capacity, and excellent in vitro targeting efficiency against 4T1-Luc cells.

NLs displayed favorable tumor-targeting properties in vivo

To investigate the tumor-targeting efficacy of NLs and LIPs towards untreated and inflamed tumor tissues respectively, we developed a tumor-bearing mouse model (pre-treated with or without phototherapy treatment) and conducted in vivo imaging experiments. It should be noted that we utilized intra-tumoral injection of CuS@BSA nanoparticles as an alternative to IR780@NLs to induce inflammation within tumor tissue after prolonged light radiation [24]. This choice is made because CuS@BSA lacks a fluorescent signal, thereby preventing any potential interference from the IR780 signal during the subsequent detection of DiR-labeled NLs or DiR-labeled

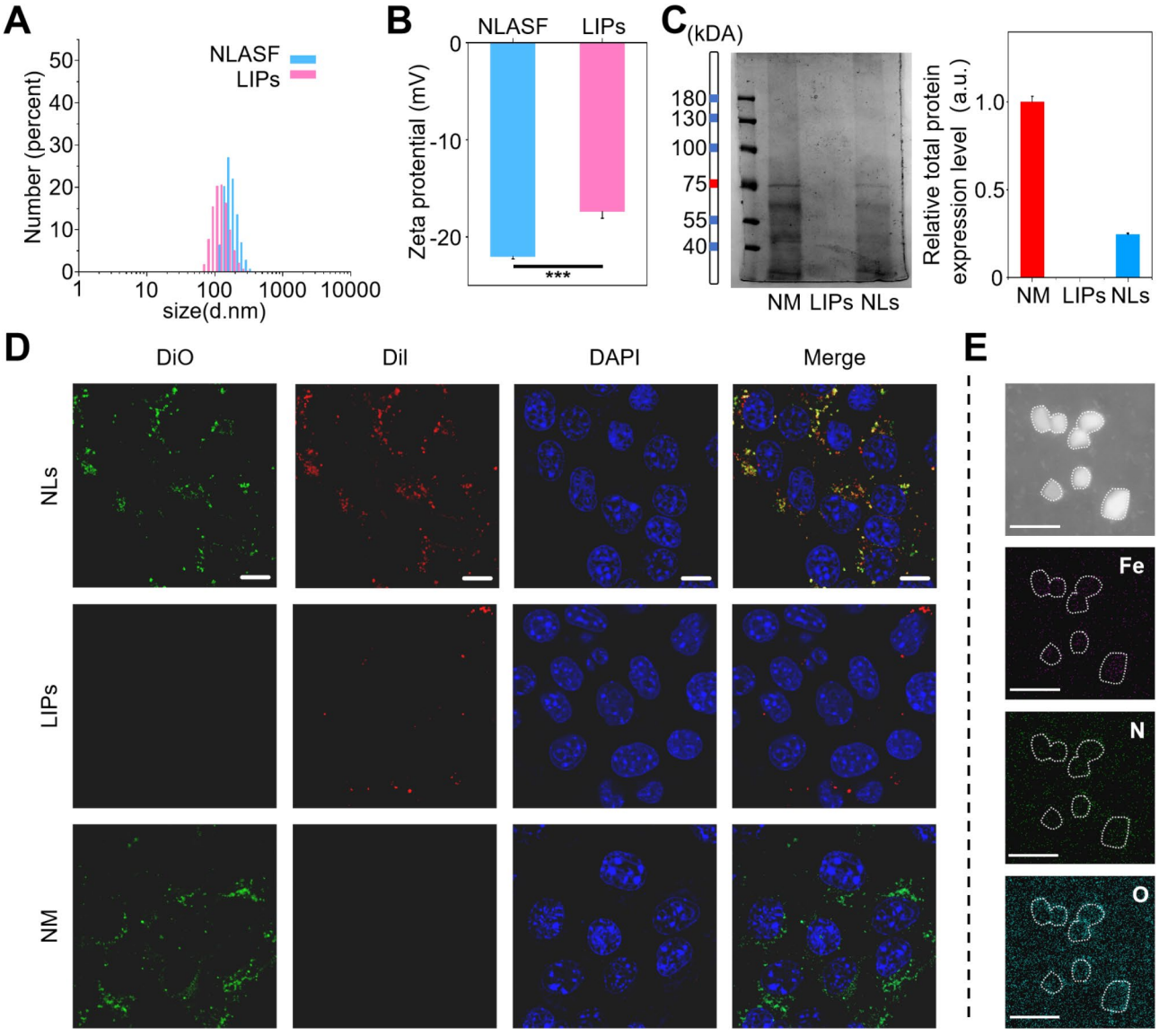

Fig. 3 Characterization of NLASF. (**A**) Size distribution and (**B**) Zeta potential of NLASF and LIPs measured by DLS. (**C**) SDS-PAGE analysis and quantitative analysis of the total proteins expressed on NM, LIPs, and NLs. (**D**) CLSM images of 4T1-Luc cells incubated with NM, LIPs, and NLs (red: Dil-labled LIPs; green: DiO-labled NM; blue: nuclei of 4T1-Luc cells). Scale bar = 10 μm. (**E**) TEM and elemental mapping images of NLASF. Scale bar = 500 nm

LIPs in vivo. Numerous studies have demonstrated that both CuS@BSA-mediated photothermal therapy (PTT) (Figure S7) and IR780-mediated PDT can induce an inflammatory response in tumor tissue [25]. Real-time fluorescence imaging demonstrated that DiR-labeled NLs (NLs@DiR) exhibited stronger tumor target enrichment compared to DiR-labeled LIPs, regardless of the application of the CuS@BSA-mediated PTT (Fig. 4A). Moreover, NLs@DiR injected after PTT exhibited a significantly enhanced tumor-targeting efficacy compared to the NLs@DiR group without receiving PTT. Isolated tumor fluorescence images and quantitative analysis at 96 h further corroborated this result (Fig. 4B C). These results demonstrated that our prepared NLs exhibit strong tumor-targeting properties in vivo, particularly against the inflamed tumor tissues.

NLASF inhibits cancer metastasis induced by platelets and ROS

Existing researches indicate that platelets play a significant role in promoting tumor EMT and metastasis [26]. Moreover, during the process of tumor metastasis, the pre-metastatic niche undergoes EMT to form mesenchymal tumor cells, which can initiate intravasation and complete the transendothelial migration [27]. As shown in Figure S8, CLSM images showed that following platelet treatment, the expression of Vimentin was upregulated while E-cadherin expression was downregulated

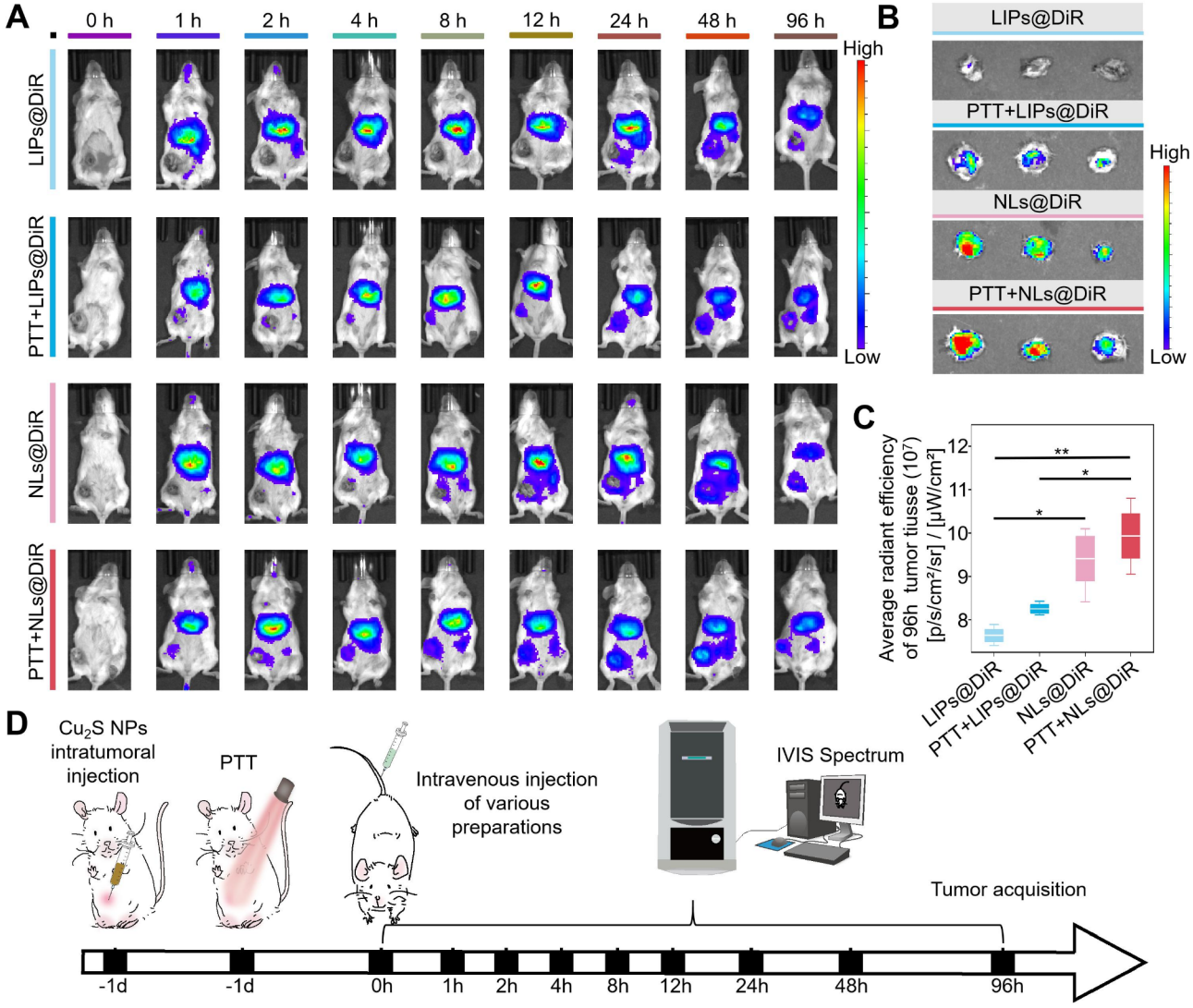

Fig. 4 Accumulation of the NLs and LIPs in the untreated and inflamed tumor tissues, respectively. (**A**) Representative fluorescence images of tumor-bearing mice following prolonged phototherapy or not at 0, 1, 2, 4, 8, 12, 24, 48, 96 h post-intravenous injection of NLs@DiR and LIPs@DiR ($n = 3$). (**B**) Fluorescence images of isolated tumor tissues 96 h post-intravenous injection of NLs@DiR and LIPs@DiR. (**C**) Quantitative analysis of fluorescence intensity of isolated tumor tissues. (**D**) Schematic diagram of the timeline for detecting tumor-targeting of NLs and its biodistribution in vivo

in 4T1-Luc cells, and this EMT state could be reversed by NLASF. Cell viability analysis revealed that synchronous treatment with 50 μg mL^{-1} of LAS and 50 μg mL^{-1} of nanozyme FeGA, as well as equal amounts of NLASF had no toxicity on 4T1-Luc and HUVEC (Fig. 5A and B). Subsequently, we simulated the migration and transendothelial migration of tumor cells using transwell experiments, where HUVEC were placed in the upper chamber to mimic the endothelial layer (Fig. 5C). Not unexpectedly, platelets promoted migration and transendothelial migration of tumor cells. Treatment with various preparations containing LAS resulted in a significant reduction in the number of tumor cells migrating to the bottom chamber, as well as the transendothelial migration efficiency (Fig. 5E).

Since platelet aggregation can create a physical barrier that protects CTCs, we subsequently investigated the antiplatelet function of NLASF. The platelets were labeled with Dil and then incubated with ADP (A platelet-activating agent that induces platelet aggregation) [28]. As indicated though white arrows, platelets exhibited significant aggregation following ADP treatment. However, following co-incubation with LAS or NLASF, the aggregation was reversed, as evidenced by the decreased mean fluorescence intensity (MFI) in the LAS and NLASF treatment groups (Fig. 5F and G and S9A). Furthermore, the in vitro experiments on platelet-tumor cell adhesion revealed that LAS and NLASF could obviously prevented platelet-tumor cell adhesion (Fig. 5H and I and S9B).

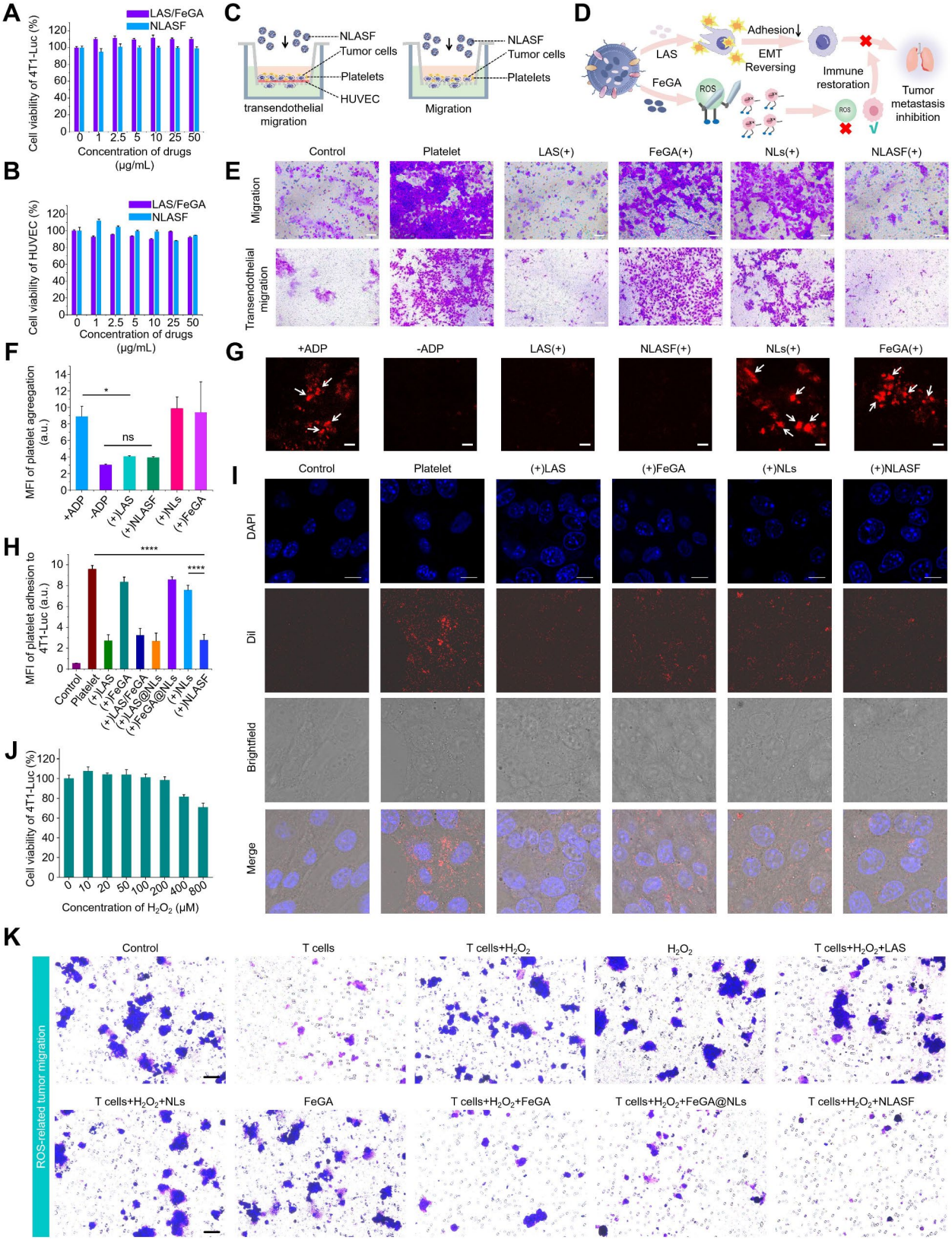

Fig. 5 (See legend on next page.)

(See figure on previous page.)

Fig. 5 Anti-metastasis effects and antiplatelet activities of NLASF in vitro. (**A**, **B**) The cell viability of 4T1-Luc, HUVEC after incubation with different concentrations of LAS/FeGA or NLASF for 24 h (CCK8 assay, $n = 3$). (**C**) Schematic diagram of the transwell experiments. (**D**) Schematic diagram of NLASF-mediated tumor metastasis suppression. (**E**) Representative transwell microscopy images of the migrated and transendothelial migrated tumor cells treated with various agents. Scale bar = 100 μm. (+) means co-incubated with platelets during various treatments. (**F**, **G**) Representative images and quantitative analysis of ADP-induced platelet aggregation following different treatments. Platelets were labeled with DiI (red), and white arrows marked the sites of platelet aggregation ($n = 3$). (+) means co-incubated with ADP during various treatments ($n = 3$). Scale bar = 50 μm. (**H**, **I**) CLSM images and quantitative analysis of platelets adhered to 4T1-Luc cells after various treatments. Nuclei: DAPI-stained (blue); Platelet: DiI-stained (red); (+) means co-incubated with platelets during various treatments. Scale bar = 10 μm. ($n = 3$). (**J**) The cell viability of 4T1-Luc after incubation with different concentrations of H_2O_2 for 24 h (CCK8 assay, $n = 3$). (**K**) Representative transwell microscopy images of ROS-induced migratory tumor cells treated with various agents Scale bar = 100 μm. [Both LAS and FeGA were concentrated at 50 μg mL^{-1} in the preparations. Legend: (*) $p < 0.05$, (**) $p < 0.01$, (***) $p < 0.001$, and (****) $p < 0.0001$]

Subsequently, in order to explore the role of ROS in tumor migration. we first measured the effect of H_2O_2 on tumor cell viability. Our results demonstrated that low concentrations of H_2O_2 induced a slight increase in the viability of 4T1-Luc cells, whereas concentrations at or above 200 μM resulted in a rapid decline in cellular activity. Therefore, 200 μm concentration of H_2O_2 was selected for the following transwell experiment to avoid directly killing tumor cells by H_2O_2. The transwell assay revealed that co-cultivation of T cells with 4T1-luc cells significantly reduced tumor cells migration. However, the addition of H_2O_2 restored the migratory capacity of tumor cells. Notably, subsequent treatment with a formulation containing antioxidant nanozyme FeGA effectively suppressed the migration of tumor cells under these conditions (Fig. 5J K). These results suggest that excessive ROS might promote tumor cells migration via compromising the cytotoxic function of T cells, and that scavenging excessive ROS by formulation containing antioxidant nanozyme FeGA can effectively inhibit tumor metastasis.

NLASF scavenges ROS and activates immune function both in vitro and in vivo

To investigate the ROS scavenging function of FeGA and NLASF, we subsequently designed a series of experiments. Chromogenic detection of ·OH was performed by using TMB [29]. Following sufficient reaction with nanozyme FeGA, the absorbance of oxidation state TMB gradually diminished with increasing concentrations of NLASF, and quantitative analysis showed that no significant difference in the effectiveness of the FeGA and NLASF in scavenging ·OH at the same concentration. Moreover, following the sufficient reaction with DPPH and ABTS probes [30, 31], which were used to evaluate antioxidant ability, it was observed that the characteristic absorption peaks of DPPH and ABTS at 517 nm and 734 nm gradually disappeared in relation to the increased concentration of nanozyme FeGA or NLASF (Figure S10, 6 A, and 6B), indicating nanozyme FeGA could be used as an antioxidant. Notably, the loading of the nanozyme FeGA into NLs does not hinder its antioxidative properties.

The redox status is essential for the activity of T cells [32]. However, high level of oxidation stress in the tumor microenvironment is detrimental for the proliferation and function of T cells. After primary T cells were co-incubated with various agents for 24 h, the CCK-8 assay results revealed that the viability of primary T cells was suppressed by H_2O_2 in a concentration-dependent manner (Fig. 6C). At the same time, as the concentration of nanozyme FeGA elevated, the viability of T cells was gradually restored. The results further revealed that H_2O_2 could suppress the enhancement of T cell proliferation induced by concanavalin A (conA) [33]. As the concentration of nanozyme FeGA elevated, the proliferation of T cells was restored (Fig. 6D and E). Moreover, our findings indicated that LAS, nanozyme FeGA, LAS/FeGA, NLs and NLASF had no toxicity on T cells at the experimental concentrations (Fig. 6C). Subsequently, we thoroughly investigated the effect of NLASF on restoring T cells functions [34]. The flow cytometry results revealed that preparations containing FeGA significantly mitigated the impairment of T cell function caused by H_2O_2, leading to significant upregulation of GZMB and IFN-γ expression (Fig. 6F-I).

To verify the in vivo antioxidant effects of nanozyme FeGA as well as NLASF, we subsequently established animal models for in vivo experiments. Following prolonged PDT, the mice were intravenously injected with different preparations. The assessment of the oxidative indicators within residual tumor tissues in situ were conducted. The results indicated that the total SOD activity of PBS-treated group was the lowest, while NLASF group exhibited the most effective restoration of total SOD level (Fig. 6J). In contrast, the relative MDA level in the PBS-treated group was the highest, however, following various treatments, MDA levels were attenuated, with the NLASF-treated group exhibiting the lowest MDA level (Fig. 6K). Bioluminescence images revealed that NLASF could significantly attenuate luminol-based chemiluminescent signal surrounding residual tumor, marking it as the lowest among the groups (Fig. 6L and S11). The fluorescence intensity of SOSG probe attenuated following various treatments, and the ROS scavenging ability of FeGA@NLs and NLASF were both significantly greater compared to the PBS group (Fig. 6N). These data

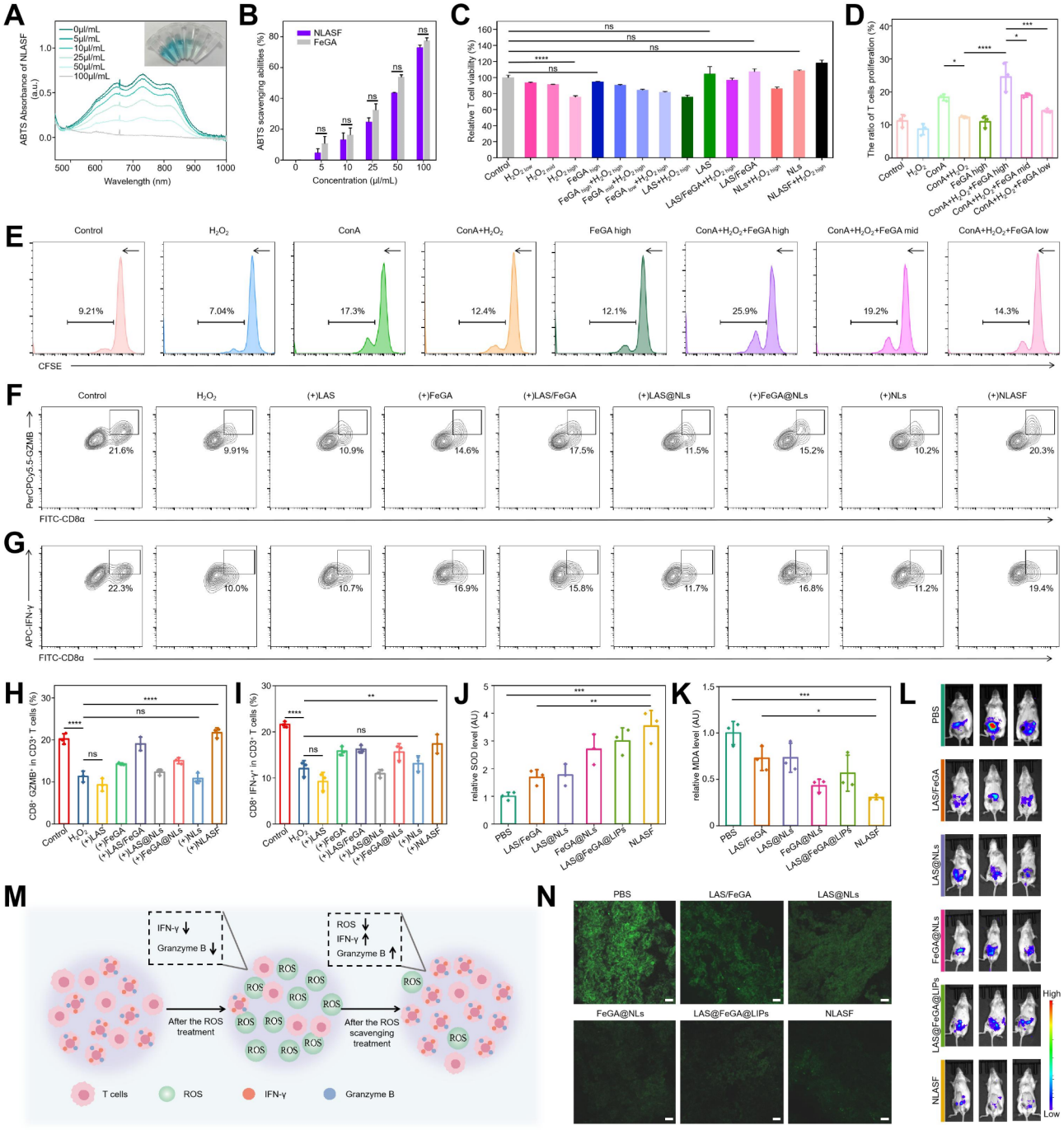

Fig. 6 Evaluation of the antioxidant effect of NLASF in vitro and in vivo and its impact on T cell function. (**A**) The UV absorption of ABTS radicals in various concentration of NLASF, accompanied by a representative image of ABTS-antioxidation assay. (**B**) Quantitative analysis of ABTS radical scavenging ratio after incubation with NLASF and FeGA ($n = 3$). (**C**) Relative T cells viabilities after various treatments (CCK-8 assay). (**D**, **E**) Flow cytometry analysis and quantitative analysis of the proliferation percent of T cells after various treatments. (**F**, **H**) Flow cytometry analysis and quantitative analysis of $CD8^+$ $GZMB^+$ in $CD3^+$ T cells expression after various treatments ($n = 3$). (**G**, **I**) Flow cytometry analysis and quantitative analysis of $CD8^+$ $IFN\text{-}\gamma^+$ in $CD3^+$ T cells expression after various treatments ($n = 3$). (**J**) Relative SOD level of tumor tissue homogenate after various treatments following prolonged PDT ($n = 3$). (**K**) Relative MDA level of tumor tissue homogenate after various treatments following prolonged PDT ($n = 3$). (**L**) Luminol bioluminescence images of tumor-bearing mice after various treatments following prolonged PDT ($n = 3$). (**M**) A diagrammatic sketch illustrates the process of ROS scavenging aimed at restoring the functionality of cytotoxic T cells. (**N**) CLSM images of tumor tissue sections detected via SOSG probe after various treatments following prolonged PDT. Scale bar = 50 μm. [Legend: (*) $p < 0.05$, (**) $p < 0.01$, (***) $p < 0.001$, and (****) $p < 0.0001$]

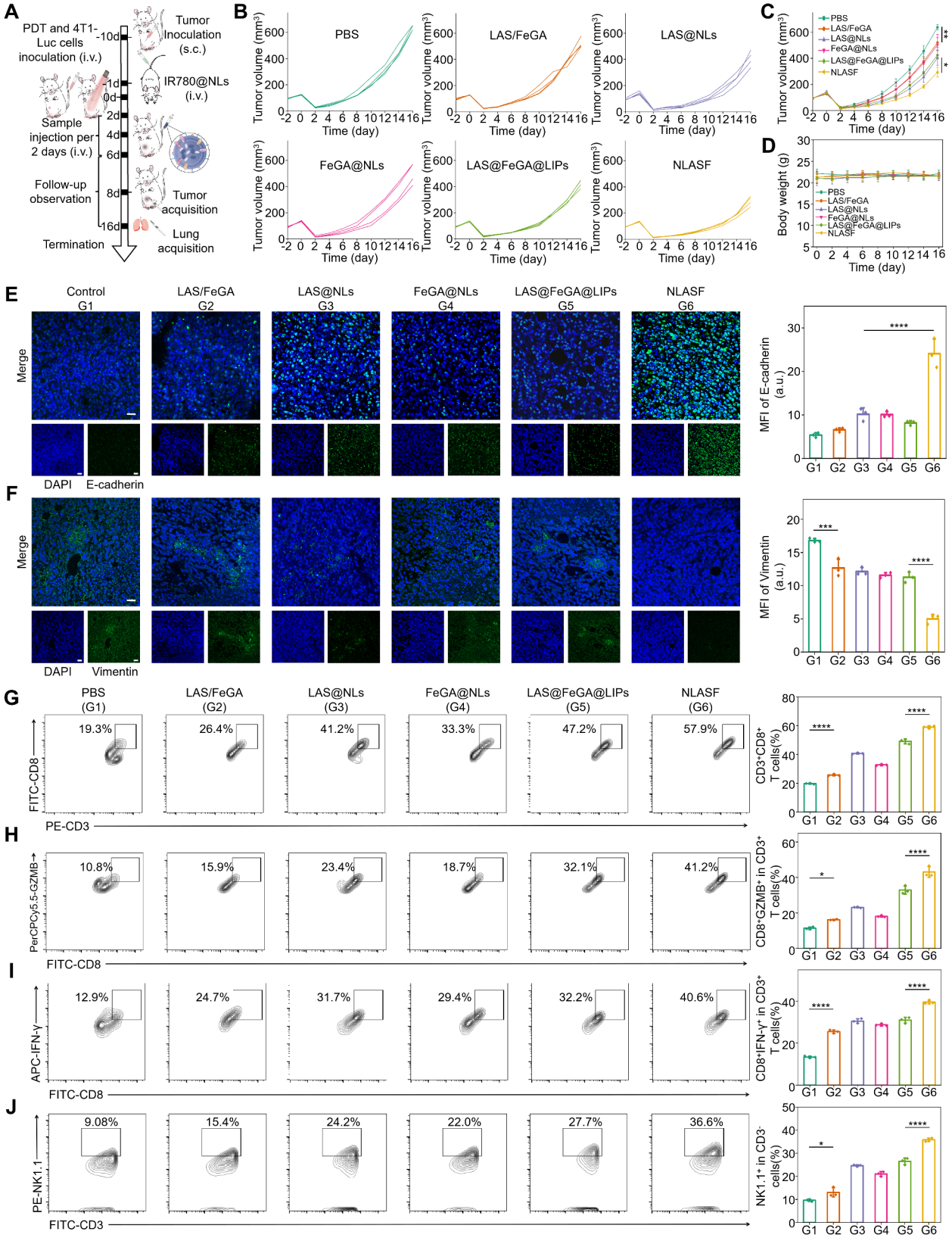

Fig. 7 (See legend on next page.)

(See figure on previous page.)

Fig. 7 In vivo antitumor and immune activation effects of NLASF. (**A**) Time curve for the construction of animal models, along with the administration of various treatments and the acquisition of tissues. (**B**) Individual tumor volumes of mice with various treatments ($n=4$). (**C**) Average tumor volumes of mice with various treatments ($n=4$). (**D**) Average body weights of mice following various treatment ($n=4$). (**E**, **F**) The EMT reversing analysis in vivo. Representative CLSM images of tumor tissue sections of tumor-bearing BALB/C mice following prolonged PDT with different treatments. Staining of (**E**) E-cadherin and (**F**) Vimentin (both green). DAPI (blue) for staining nucleus. Scale bar = 50 μm. (**G**-**I**) Analysis of immune cell infiltration of each group in orthotopic tumor tissues. $CD3^+CD8^+$ cells (panel (**G**)); $CD8^+GZMB^+$ in $CD3^+$ T cells (panel (**H**)); $CD8^+IFN\text{-}\gamma^+$ in $CD3^+$ T cells (panel (**I**)); $NK1.1^+$ in $CD3^-$ cells (panel (**J**)) ($n=3$). [Legend: (*) $p<0.05$, (**) $p<0.01$, (***) $p<0.001$, and (****) $p<0.0001$]

revealed that nanozyme FeGA had redox regulation ability both in vitro and in vivo, and this effect was enhanced when it was incorporated into NLs. Following the scavenging of ROS, the viability, proliferation, and functionality of T cells were restored (Fig. 6M).

The antitumor and immune activation effect of NLASF in vivo following prolonged PDT

To further verify the effects of NLASF on antitumor activity and immune activation, we established a tumor-bearing mice model. Following prolonged PDT in each group, the mice were intravenously injected with different preparations (Fig. 7A). During the treatment period, there were significant difference in tumor recurrence volume. Notably, following NLASF treatment, tumor recurrence was significantly suppressed, resulting in the lowest average tumor volume compared to the other groups (Fig. 7B C). At the same time, no significant changes in the body weight of the mice were observed, indicating that the preparations we developed exert negligible adverse effects on mouse growth (Fig. 7D). Moreover, CLSM images revealed that following various treatments, the expression of Vimentin was downregulation, while E-cadherin was upregulation, and the NLASF-treated group demonstrated the most pronounced effect in reversing tumor EMT (Fig. 7E F).

We further investigated the impact of the combination therapy nanoplatform on the tumor immune microenvironment (TIME) [35–37]. After various treatments, the infiltration of $CD3^+CD8^+$ T cells in orthotopic tumors was increased, accompanied by an upregulation of IFN-γ and GZMB-positive $CD8^+$ T cells, with the NLASF-treated group showing the highest expression levels (Fig. 7G-I). In contrast, the infiltration of immunosuppressive tumor-associated macrophages, MDSCs, and T_{reg} cells decreased, with the NLASF-treated group showing the most pronounced inhibitory effect on these immunosuppressive cells (Figure S12). NK cells play a crucial role in the immune response against malignant tumor by directly killing tumor cells. However, the high ROS environment can induce NK cells dysfunction. Following various treatments, flow analysis showed $NK1.1^+$ cells among $CD3^-$ populations were increased, with the highest expression level observed in the NLASF treatment group (Fig. 7J).

The above results demonstrated that the combination therapy nanoplatform NLASF could not only inhibit oxidative stress and EMT induced by prolonged PDT, but also reverse the immunosuppressive TIME.

Lung metastasis was suppressed by NLASF following prolonged PDT treatment

Encouragingly, the NLASF group has shown excellent effect in inhibiting EMT and reversing the immunosuppressive TIME following prolonged PDT. We then examined whether tumor lung metastasis was also reduced after treatment with NLASF. Lung tissues were obtained to analyze tumor metastasis on day 16. Following prolonged PDT, the untreated group exhibited the highest number of pulmonary metastatic nodules, whereas the NLASF-treated group displayed a markedly reduced number of metastatic nodules (Fig. 8A). Real-time bioluminescence images of lung tissues on days 8 and 16 also revealed that the PBS group exhibited the most severe tumor metastasis, while following NLASF treatment, lung metastasis was nearly eliminated (Fig. 8B). H&E staining analysis corroborated these findings (Fig. 8C). To further elucidate the mechanisms underlying the inhibition of metastasis, we also investigated the proportions of tumor-associated macrophages, MDSCs, $CD8^+$ T cells, T_{regs}, and NK cells in the lung tissue following various treatments. Encouragingly, the proportion of immunosuppressive tumor-associated macrophages, MDSCs and T_{regs} were significantly reduced after NLASF treatment (Fig. 8D-F). In contrast, the populations of $CD3^+CD8^+$ T cells and $NK1.1^+$ cells in the $CD3^-$ fraction were significantly increased (Figure S13). In short, the combination therapy nanoplatform NLASF effectively inhibited the EMT of the primary tumors and reversed immune suppression in the lung tissues, thereby inhibiting the formation of pulmonary metastasis.

In vivo safety evaluation of NLASF

To evaluate the safety of NLASF for systemic application, we performed a safety evaluation in orthotopic tumor-bearing mice. The tail bleeding assay [38] and hematological revealed that treatment with free LAS/FeGA resulted in significant bleeding and thrombocytopenia compared to the other groups (Figure S14). We attributed this condition to the hematological toxicity associated with the free antiplatelet agent LAS. These results illuminated that utilizing NLs to encapsulate free LAS could effectively attenuate its analysis hematological toxicity. Moreover, analysis of the routine plasma biochemical examinations

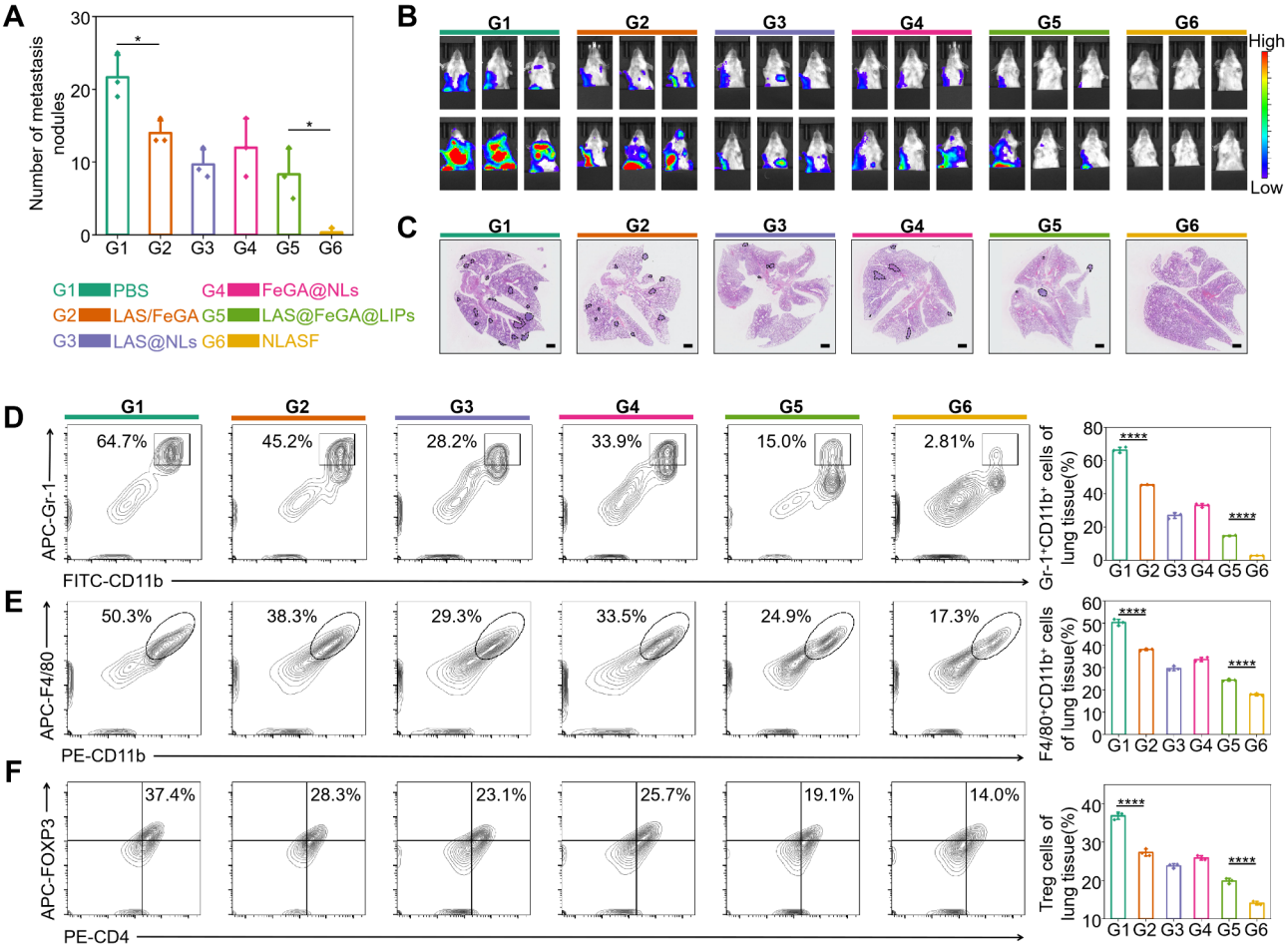

Fig. 8 In vivo anti-metastasis effects of NLASF and analysis of immune microenvironment in lung tissues. (**A**) Number of metastasis lung nodules after various treatments ($n=3$). (**B**) Realtime bioluminescence images of lung metastasis on days 8 and 16 after various treatments ($n=3$). (**C**) H&E analysis of lung tissues of various treatments groups ($n=3$). (**D**-**F**) Analysis of immune cell infiltration of each group in lung tissues. $CD11b^+Gr\text{-}1^+$ cells (panel (**D**)); $CD11b^+F4/80^+$ cells (panel (**E**)); $CD4^+FOXP3^+$ cells (panel (**F**)) ($n=3$). [Legend: (*) $p<0.05$, (**) $p<0.01$, (***) $p<0.001$, and (****) $p<0.0001$]

also revealed the safety of NLs-coated nanodrugs (Figure S15). The H&E staining results further illustrated that there were no evident irregularities in the major organs (heart, liver, spleen, and kidneys) of all groups (Figure S16). In general, the neutrophil membrane-fused liposomal nanoplatform we synthesized exhibited significant biocompatibility and safety, with no hematological toxicity or organic lesions.

Conclusion

In this study, we initially employed a straightforward approach that involved extending the duration of PDT to enhance its efficacy. Our results further indicated that extending the duration of PDT generates a significant amount of ROS, which facilitates the EMT of tumor cells and ultimately promotes tumor cell metastasis, aided by platelets. We subsequently extracted the neutrophil membrane to develop a lipid nanoplatform NLs aimed at the targeted delivery of the antioxidant nanozyme FeGA and the antiplatelet drug LAS. In addition, the introduction of this nanoplatform NLASF significantly decreases the in vivo toxicity associated with free LAS. Experimental results indicated that the EMT of tumor cells and the immunosuppressive microenvironment of tumor tissue can be effectively reversed by treatment with NALSF, thereby inhibiting lung metastasis of tumors after prolonged PDT. In summary, this study confirms that the combination of redox regulation and antiplatelet therapy via NLASF represents a promising therapeutic strategy for the prevention of PDT-induced tumor metastasis.

Supplementary Information

The online version contains supplementary material available at https://doi.org/10.1186/s12951-025-03332-y.

Supplementary Material 1

Acknowledgements
Not applicable.

Author contributions
Z.S., Q.S. and W.Y contributed equally to this work. Z.S., Q.S. and W.Y. conceived this work. Z.S., Q.S., W.Y. and D.Y. designed, prepared, and characterized the materials. Z.S., Q.S., W.Y., C.H., and C.C. carried out the in vitro, ex vivo, and in vivo experiments. Z.S., Q.S., W.Y., Y.L. and K.L. analyzed the data and discussed the results. Z.S., Q.S., W.Y., and W.S. wrote and edited the manuscript. Y.L., C.H., C.C. and K.L. reviewed the manuscript. D.Y. and Y.Y. supervised the project. The manuscript was written through contributions of all authors. All authors have given approval for the final version of the manuscript.

Funding
This study was supported by the key project of the Anhui Provincial Department of Education (2022AH040077 and 2022AH040080), the Academic Funding Project for Top-Notch Talents in Anhui Province (gxbjZD2022027), The Open Fund of High-level Key Discipline of Chemistry of Chinese Medicine of the State Administration of Traditional Chinese Medicine, Anhui University of Chinese Medicine (HKDCCM2024017), Scientific Research Team Program of Anhui Colleges and Universities (2022AH010036), the Excellent Youth Fund Project of Anhui Provincial Department of Education (2023AH030065).

Data availability
No datasets were generated or analysed during the current study.

Declarations

Ethics approval and consent to participate
Six-weeks old female BALB/c mice (18–22 g) were ordered from Ziyuan Laboratory Animal Technology Co. Ltd (Hangzhou, China). All Mice were housed and cared in a room with a temperature around 20–22 ℃ and a 12-h light/ 12-h dark cycle. All animal experiments were performed according to animal care regulations and the Ethics Committee of the Anhui University of Chinese Medicine. (AHUCM- mouse-2024203)

Consent for publication
All authors of this study agreed to publish.

Competing interests
The authors declare no competing interests.

Author details
[1]School of Pharmacy, Anhui University of Chinese Medicine, #1 Qian Jiang Road, Hefei 230031, Anhui, PR China
[2]Anhui Province Key Laboratory of Pharmaceutical Preparation Technology and Application, Hefei 230031, China
[3]Anhui Provincial Key Laboratory of Chinese Medicinal Formula, Hefei 230021, China
[4]Engineering Technology Research Center of Modernized Pharmaceutics, Anhui Education Department (AUCM), Hefei 230012, China

Received: 4 February 2025 / Accepted: 14 March 2025
Published online: 04 April 2025

References

1. Correia JH, Rodrigues JA, Pimenta S, Dong T, Yang Z. Photodynamic therapy review: principles, photosensitizers, applications, and future directions. Pharmaceutics. 2021;13:1332.
2. Chen A, Huang H, Fang S, Hang Q. ROS: A booster for chronic inflammation and tumor metastasis. Biochim Biophys Acta Rev Cancer. 2024;1879:189175.
3. Shah R, Ibis B, Kashyap M, Boussiotis VA. The role of ROS in tumor infiltrating immune cells and cancer immunotherapy. Metabolism. 2024;151:155747.
4. Chatterjee R, Chatterjee J. ROS and oncogenesis with special reference to EMT and stemness. Eur J Cell Biol. 2020;99:151073.
5. Goh J, Enns L, Fatemie S, Hopkins H, Morton J, Pettan-Brewer C, Ladiges W. Mitochondrial targeted catalase suppresses invasive breast cancer in mice. BMC Cancer. 2011;11:191.
6. van Rossen ME, Sluiter W, Bonthuis F, Jeekel H, Marquet RL, van Eijck CH. Scavenging of reactive oxygen species leads to diminished peritoneal tumor recurrence. Cancer Res. 2000;60:5625–9.
7. Ishikawa K, Takenaga K, Akimoto M, Koshikawa N, Yamaguchi A, Imanishi H, Nakada K, Honma Y, Hayashi J. ROS-generating mitochondrial DNA mutations can regulate tumor cell metastasis. Science. 2008;320:661–4.
8. Shi Q, Ji T, Tang X, Guo W. The role of tumor-platelet interplay and micro tumor thrombi during hematogenous tumor metastasis. Cell Oncol Dordr Neth. 2023;46:521–32.
9. Gasic GJ, Gasic TB, Stewart CC. Antimetastatic effects associated with platelet reduction. Proc. Natl. Acad. Sci. U. S. A. 1968;61:46–52.
10. Schlesinger M. Role of platelets and platelet receptors in cancer metastasis. J Hematol Oncol J Hematol Oncol. 2018;11:125.
11. Wang X, Zhao S, Wang Z, Gao T. Platelets involved tumor cell EMT during circulation: communications and interventions. Cell Commun Signal CCS. 2022;20:82.
12. Jelic MD, Mandic AD, Maricic SM, Srdjenovic BU. Oxidative stress and its role in cancer. J Cancer Res Ther. 2021;17:22–8.
13. Oberley LW, Buettner GR. Role of superoxide dismutase in cancer: a review. Cancer Res. 1979;39:1141–9.
14. Valadez-Cosmes P, Raftopoulou S, Mihalic ZN, Marsche G, Kargl J. Myeloperoxidase: growing importance in cancer pathogenesis and potential drug target. Pharmacol Ther. 2022;236:108052.
15. Gross S, Gammon ST, Moss BL, Rauch D, Harding J, Heinecke JW, Ratner L, Piwnica-Worms D. Bioluminescence imaging of myeloperoxidase activity in vivo. Nat Med. 2009;15:455–61.
16. Sharma SK, Hamblin MR. The use of fluorescent probes to detect ROS in photodynamic therapy. Methods Mol Biol Clifton NJ. 2021;2202:215–29.
17. van der Leun AM, Thommen DS, Schumacher TN. CD8 + T cell States in human cancer: insights from single-cell analysis. Nat Rev Cancer. 2020;20:218–32.
18. Liu JL, Xu X, Rixiati Y, Wang CY, Ni HL, Chen WS, Gong HM, Zhang ZL, Li S, Shen T, Li JM. Dysfunctional circadian clock accelerates cancer metastasis by intestinal microbiota triggering accumulation of myeloid-derived suppressor cells. Cell Metab. 2024;36:1320–e13349.
19. Odero-Marah V, Hawsawi O, Henderson V, Sweeney J. Epithelial-Mesenchymal Transition (EMT) and Prostate Cancer. In: Schatten, H, editor Cell & Molecular Biology of Prostate Cancer. 2018; 101–110.
20. Dong X, Gao J, Zhang CY, Hayworth C, Frank M, Wang Z. Neutrophil Membrane-Derived nanovesicles alleviate inflammation to protect mouse brain injury from ischemic stroke. ACS Nano. 2019;13:1272–83.
21. Du Y, Huo Y, Yang Q, Han Z, Hou L, Cui B, Fan K, Qiu Y, Chen Z, Huang W, et al. Ultrasmall iron-gallic acid coordination polymer nanodots with antioxidative neuroprotection for PET/MR imaging-guided ischemia stroke therapy. Explor Beijing China. 2023;3:20220041.
22. Vivas D, Martín A, Bernardo E, Ortega-Pozzi MA, Tirado G, Fernández C, Vilacosta I, Núñez-Gil I, Macaya C, Fernández-Ortiz A. Impact of intravenous lysine acetylsalicylate versus oral aspirin on Prasugrel-Inhibited platelets: results of a prospective, randomized, crossover study (the ECCLIPSE Trial). Circ Cardiovasc Interv. 2015;8:e002281.
23. Qiao Q, Liu X, Cui K, Li X, Tian T, Yu Y, Niu B, Kong L, Yang C, Zhang Z. Hybrid biomimetic nanovesicles to drive high lung biodistribution and prevent cytokine storm for ARDS treatment. ACS Nano. 2022;16:15124–40.
24. Dun X, Liu S, Ge N, Liu M, Li M, Zhang J, Bao H, Li B, Zhang H, Cui L. Photothermal effects of CuS-BSA nanoparticles on H22 hepatoma-bearing mice. Front Pharmacol. 2022;13:1029986.
25. Maeding N, Verwanger T, Krammer B. Boosting Tumor-Specific immunity using PDT. Cancers. 2016;8:91.
26. Zhou L, Zhang Z, Tian Y, Li Z, Liu Z, Zhu S. The critical role of platelet in cancer progression and metastasis. Eur J Med Res. 2023;28:385.
27. Zhang D, Bi J, Liang Q, Wang S, Zhang L, Han F, Li S, Qiu B, Fan X, Chen W, et al. VCAM1 promotes tumor cell invasion and metastasis by inducing EMT and transendothelial migration in colorectal cancer. Front Oncol. 2020;10:1066.
28. Li S, Li L, Lin X, Chen C, Luo C, Huang Y. Targeted Inhibition of tumor inflammation and tumor-Platelet crosstalk by Nanoparticle-Mediated drug delivery mitigates cancer metastasis. ACS Nano. 2022;16:50–67.
29. Zhu W, Liu YQ, Liu P, Cao J, Shen AG, Chu PK. Blood-Glucose-Depleting hydrogel dressing as an activatable photothermal/chemodynamic antibacterial agent for healing diabetic wounds. ACS Appl Mater Interfaces. 2023;15:24162–74.
30. Tsai CE, Lin LH. DPPH scavenging capacity of extracts from camellia seed Dregs using polyol compounds as solvents. Heliyon. 2019;5:e02315.

31. Re R, Pellegrini N, Proteggente A, Pannala A, Yang M, Rice-Evans C. Antioxidant activity applying an improved ABTS radical cation decolorization assay. Free Radic Biol Med. 1999;26:1231–7.
32. Gambhir L, Sharma V, Kandwal P, Saxena S. Perturbation in cellular redox homeostasis: decisive regulator of T cell mediated immune responses. Int Immunopharmacol. 2019;67:449–57.
33. Gantner F, Leist M, Lohse AW, Germann PG, Tiegs G. Concanavalin A-induced T-cell-mediated hepatic injury in mice: the role of tumor necrosis factor. Hepatol Baltim Md. 1995;21:190–8.
34. Hodge G, Barnawi J, Jurisevic C, Moffat D, Holmes M, Reynolds PN, Jersmann H, Hodge S. Lung cancer is associated with decreased expression of Perforin, granzyme B and interferon (IFN)-γ by infiltrating lung tissue T cells, natural killer (NK) T-like and NK cells. Clin Exp Immunol. 2014;178:79–85.
35. Fu T, Dai LJ, Wu SY, Xiao Y, Ma D, Jiang YZ, Shao ZM. Spatial architecture of the immune microenvironment orchestrates tumor immunity and therapeutic response. J Hematol Oncol J Hematol Oncol. 2021;14:98.
36. Rui R, Zhou L, He S. Cancer immunotherapies: advances and bottlenecks. Front Immunol. 2023;14:1212476.
37. Hofer F, Di Sario G, Musiu C, Sartoris S, De Sanctis F, Ugel S. A complex metabolic network confers immunosuppressive functions to Myeloid-Derived suppressor cells (MDSCs) within the tumour microenvironment. Cells. 2021;10:2700.
38. Luo L, Zhang B, Tao F, Chen Z, Ye Q, Zhao X, Wu J. Perfluorotributylamine-Loaded albumin nanoparticles downregulate Platelet-Derived TGFβ to inhibit tumor metastasis. ACS Nano. 2023;17:15388–400.

Publisher's note

Springer Nature remains neutral with regard to jurisdictional claims in published maps and institutional affiliations.